Anisotropic Strain Limiting

F. Hernandez, G. Cirio, A.G. Perez, and M.A. Otaduy

URJC Madrid, Spain

Abstract

Many materials exhibit a highly nonlinear elastic behavior, such as textiles or finger flesh. An efficient way of enforcing the nonlinearity of these materials is through strain-limiting constraints, which is often the model of choice in computer graphics. Strain-limiting allows to model highly non-linear stiff materials by eliminating degrees of freedom from the computations and by enforcing a set of constraints. However, many nonlinear elastic materials, such as composites, wood or flesh, exhibit anisotropic behaviors, with different material responses depending on the deformation direction. This anisotropic behavior has not been addressed in the past in the context of strain limiting, and naïve approaches, such as applying a different constraint on each component of the principal axes of deformation, produce unrealistic results. In this paper, we enable anisotropic behaviors when using strain-limiting constraints to model nonlinear elastic materials. We compute the limits for each principal axis of deformation through the rotation and hyperbolic projection of the deformation limits defined in the global reference frame. The limits are used to formulate the strain-limiting constraints, which are then seamlessly combined with frictional contact constraints in a standard constrained dynamics solver.

Categories and Subject Descriptors (according to ACM CCS): I.3.5 [Computer Graphics]: Physically based modeling—

1. Introduction

Highly nonlinear elastic materials, such as flesh and fabrics, can be modeled very accurately using hyperelasticity. However, hyperelastic models exhibit a very high numerical stiffness, which requires very small simulation time steps. An efficient alternative to hyperelasticity is the use of strain-limiting constraints. In essence, strain-limitig eliminates degrees of freedom from the computations and, as a counterpart, enforces a set of constraints. Therefore, strain-limiting methods enable larger time steps, and turn the complexity into the enforcement of constraints. They are often the model of choice for highly nonlinear elasticity in computer graphics [Pro95, BMF03, TPS09].

Many nonlinear stiff materials exhibit anisotropic behaviors. Wood, for instance, has different deformation and strength properties along three clearly defined directions: longitudinal (parallel to the grain), radial (across the growth rings) and tangential (tangent to the growth rings). Muscles are anisotropic, with different properties according to the direction of the muscular fibers. When modeling heterogeneous objects through a single mesh, such as a human fin-

ger, the presence of flesh, skin and bones generates a highly nonlinear and anisotropic behavior, with different amounts of deformation depending on the position and direction of the applied loads.

This anisotropic behavior has not been addressed in the past in the context of constraint-based strain limiting. If setting up common limits for all possible directions is a solved problem, it is not clear how to set diverse limits for arbitrary directions. There are simple and straightforward approaches used in other contexts to model anisotropy, such as projecting the principal deformations onto orthogonal directions, or computing linear interpolation of limits defined for fixed orthogonal directions. However, these solutions produce unrealistic results due to over- or under-constrained axes.

In this paper, we introduce a novel hyperbolic projection function to compute stretch and compress limits along any deformation direction, and formulate the strain-limiting constraints based on this interpolation. Since we enforce the constraints following a constrained optimization formulation, we show how to compute the jacobians of the constraints w.r.t. the generalized coordinates of the system.

Strain-limiting and frictional contact constraints are then seamlessly combined in a standard constrained dynamics solver. We compare our approach to naïve solutions and different approaches found in the literature, and show that our approach produces predictable and more realistic results.

2. Related Work

Strain-limiting was initially applied to cloth simulation based on the mass-spring model [Pro95, BMF03], and later extended to finite element methods [TPS09], where strain is measured and later limited by computing a correcting velocity vector that enforces the strain limits on each component. Wang et al. [WOR10] propose an approach independent from the underlying parametrization by computing the principal strains of each mesh element, which are later constrained to predefined limits in an isotropic fashion. They also improve the convergence of relaxation compared to [TPS09] by following a multi-resolution scheme. Principal strains are also computed for the simulation of invertible hyperelastic materials [ITF04], and gradients of principal strains are needed for robust implicit integration of such hyperelastic materials [SZL*11]. Recently, Perez et al. [PCH*13] proposed to directly constrain the deformation tensor, and satisfy strain-limiting constraints using a Lagrange-multiplier formulation. Such a formulation leverages implicit integration, which makes the relaxation steps global and improves convergence, and treats strain-limiting constraints just like other constraints such as contact, allowing them to be solved simultaneously using standard solvers.

The anisotropic behavior of real-world hyperelastic materials has been scarcely addressed in the past in the context of strain limiting, yet many materials exhibit different material responses depending on the deformation direction. Anisotropic behaviors are hard to implement in edge-based strain-limiting approaches [Pro95, BMF03], since edges need to be aligned with the deformation direction that is being constrained, requiring extensive remeshing. In continuum-based approaches, Thomaszewski et al. [TPS09] use different limits for each strain value component of a cloth simulation (weft, warp and shear strains). With this approach, limits and strain values are always defined on undeformed axes, hence they do not distinguish well the various deformation modes under large deformations. Picinbono et al. [PDA03] allow transverse anisotropic strain-limiting (with a transverse and a radial privileged direction) by adding an energy term to a hyperalasticity formulation, penalizing stretch deformations in the transverse direction. This formulation does not suffer from the same problems as full anisotropy, since strain-limiting is only enforced on one axis, the radial axis being free to deform. Therefore, no interpolation is required, but only a projection of the strain tensor along the transverse direction.

Anisotropy behaviors can also be found in other dynamic phenomena. For instance, in the context of anisotropic fracture propagation, Allard et al. [AMC09] define two fracture stress thresholds in reference orthogonal directions. In order to define the threshold for other directions, they interpolate between the reference thresholds based on the angle between directions, and favor directions close to the reference by using a peak function with a controllable steepness.

In Wang et al. [WOR10], as well as our previous approach [PCH*13], strain limiting is achieved by constraining principal strains with given maximal and minimal values. These two approaches are therefore isotropic. In order to make them anisotropic, in this paper we design a novel hyperbolic projection function for stretch and compress limits for any deformation direction, and we take into account the resulting constraint formulation in our implicit solver.

3. Formulation of Anisotropic Strain Limiting

In this section, we present our formulation of anisotropic strain limiting using a hyperbolic projection method. We first recall the formulation of strain-limiting, which limits the principal axes of deformation inside each tetrahedron. We then define the problem of computing strain limits along arbitrary directions, and present our solution using hyperbolic projection. We also formulate the strain-limiting constraints using these anisotropic limits and describe the computation of constraint Jacobians, necessary for the constrained optimization solver.

3.1. Basic Formulation of Strain Limiting

As the underlying elasticity model, we use a linear co-rotational strain formulation [MG04] with a linear Hookean material model. We discretize the continuum elasticity equations using the finite element method (FEM) and a tetrahedral mesh with linear basis functions. With these assumptions, the strain and stress tensors are constant inside each tetrahedral element.

Given the four nodes $\{\mathbf{x}_1, \mathbf{x}_2, \mathbf{x}_3, \mathbf{x}_4\}$ of a tetrahedral element, we define its volume matrix

$$\mathbf{X} = \begin{pmatrix} \mathbf{x}_1 - \mathbf{x}_4 & \mathbf{x}_2 - \mathbf{x}_4 & \mathbf{x}_3 - \mathbf{x}_4 \end{pmatrix}. \tag{1}$$

For convenience, we express the inverse of the rest-state volume matrix based on its rows:

$$\mathbf{X}_0^{-1} = \begin{pmatrix} \mathbf{r}_1 \\ \mathbf{r}_2 \\ \mathbf{r}_3 \end{pmatrix}. \tag{2}$$

It is also convenient to define a fictitious row $\mathbf{r}_4 = -(\mathbf{r}_1 + \mathbf{r}_2 + \mathbf{r}_3)$.

Using the volume matrix, the deformation gradient $\mathbf{G} = \frac{\partial \mathbf{x}}{\partial \mathbf{x}_0}$ of a tetrahedron can be computed as

$$\mathbf{G} = \mathbf{X}\mathbf{X}_0^{-1}. \tag{3}$$

Following Perez et al. [PCH*13], we limit strain effectively by limiting the deformation gradient of each tetrahedron in the finite element mesh. To this end, we compute a singular value decomposition (SVD) of the deformation gradient of each tetrahedron:

$$\mathbf{G} = \mathbf{U}\mathbf{S}\mathbf{V}^T \ \Rightarrow \ \mathbf{S} = \begin{pmatrix} s_1 & 0 & 0 \\ 0 & s_2 & 0 \\ 0 & 0 & s_3 \end{pmatrix} = \mathbf{U}^T \mathbf{G} \mathbf{V}, \quad (4)$$

where the singular values $\{s_1, s_2, s_3\}$ capture deformations along principal axes. $\mathbf{U}$ and $\mathbf{V}$ are rotation matrices, and $\mathbf{S}$ is a scaling matrix. Unit singular values in all directions (i.e., $s_i = 1$) imply no deformation. We enforce strain limiting by applying a lower limit $s_{\min}$ (i.e., compression constraint) and an upper limit $s_{\max}$ (i.e., stretch constraint) on each singular value of the deformation gradient:

$$s_{\min} \le s_i \le s_{\max}. \quad (5)$$

3.2. Definition of Strain Limits

In the isotropic case, computing the limits for any principal axis of deformation is straightforward, since the limits are all the same no matter the direction. In the anisotropic case, however, limits and deformation values are defined on different sets of axes. Stretch and compress limits are defined on each axis of the global reference frame ($s_{\max}^j$ and $s_{\min}^j$, with $j \in \{1, 2, 3\}$). Deformation values are defined along the principal axes of deformation computed through the SVD (s_i, with $i \in \{1, 2, 3\}$). In general, the frames do not match. Yet, we need to know the value of stretch and compress limits along the principal axes of deformation to be able to formulate the constraints as in Eq. (5). In the following, we describe our method for the computation of deformation limits along the principal axes from deformation limits given on a global frame.

Fig. 1 illustrates the problem and our solution. Let F_d be the orthonormal frame representing the principal axes of deformation. According to the SVD decomposition in Eq. (4), in order to transform a vector from the global frame (where the limits are defined) to the frame F_d (where the deformation values are defined), the vector has to be rotated by matrix $\mathbf{V}^T$. Since the limits are defined on the global frame, which uses a canonical basis ($\mathbf{e}_1 \ \mathbf{e}_2 \ \mathbf{e}_3$), $\mathbf{V}^T$ provides the three directions along which the limits are known in F_d. However, the deformation values to be limited are known along the axes of F_d. Hence, our problem is reduced to finding what the limits are along these axes.

For the general case, we require a function p that projects each rotated limit onto the axes of F_d, thus providing stretch and compress limits to apply to each deformation value s_i. Since there are three directions ($\mathbf{e}_1 \ \mathbf{e}_2 \ \mathbf{e}_3$) with two limits each (stretch and compress), and each direction has to be projected on each axis of F_d, there is a total of 18 limits to be computed (6 for each deformation value s_i).
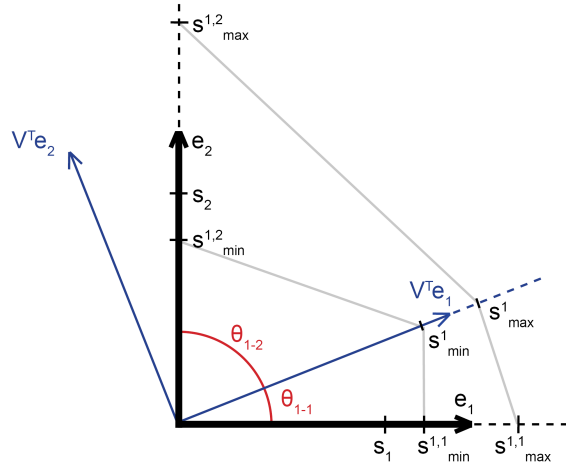

Figure 1: *Illustration of our hyperbolic projection method, which projects the limits from the rotated global axes onto the principal axes of deformation.*

3.3. Hyperbolic Projection Function

Naïve approaches for p, such as orthogonal projection or linear interpolation, result in incorrect or unrealistic results, as shown later in Section 5. Naturally, we want a non-linear interpolation where the limit remains unchanged if deformation and limit directions match, and where the limit vanishes (i.e. becomes infinitely large) when deformation and limit directions are orthogonal. Therefore, we define p as:

$$p(\theta) = \frac{1}{|cos(\theta)|}, \quad (6)$$

where θ is the angle between a given rotated limit direction and a given axis of F_d, as illustrated in Fig. 1.

Let us consider, for instance, axis $\mathbf{e}_j$ of the global frame, where $s_{\min}^j$ and $s_{\max}^j$ are defined. The limit direction in F_d is $\mathbf{V}^T \mathbf{e}_j$, and the axes of F_d are $((1,0,0)^T \ (0,1,0)^T \ (0,0,1)^T) = (\mathbf{e}_1 \ \mathbf{e}_2 \ \mathbf{e}_3)$. This results in the following stretch and compress values for each deformation value s_i:

$$s_{\min}^{j,i} = 1 + \frac{s_{\min}^j - 1}{|\mathbf{e}_i^T \mathbf{V}^T \mathbf{e}_j|}, \quad (7)$$

$$s_{\max}^{j,i} = 1 + \frac{s_{\max}^j - 1}{|\mathbf{e}_i^T \mathbf{V}^T \mathbf{e}_j|}. \quad (8)$$

Eqs. (7)-(8) provide stretch and compress values for each limit defined on a global axis ($j \in \{1, 2, 3\}$) and each principal axis of deformation ($i \in \{1, 2, 3\}$).

3.4. Constraint Formulation

In the isotropic case, the constraints are defined as:

$$C_{\min}^i = s_i - s_{\min} \geq 0, \qquad (9)$$

$$C_{\max}^i = s_{\max} - s_i \geq 0. \qquad (10)$$

Based on Eqs. (7)-(8), we reformulate our constraints to take into account each interpolated limit, resulting in:

$$C_{\min}^{j,i} = |\mathbf{e}_i^T \mathbf{V}^T \mathbf{e}_j|(s_i - 1) - (s_{\min}^j - 1) \geq 0, \qquad (11)$$

$$C_{\max}^{j,i} = (s_{\max}^j - 1) - |\mathbf{e}_i^T \mathbf{V}^T \mathbf{e}_j|(s_i - 1) \geq 0. \qquad (12)$$

3.5. Constraint Jacobians

We enforce strain limiting constraints following a constrained optimization formulation [PCH*13], summarized later in Section 4. This formulation requires the computation of constraint Jacobians w.r.t. the generalized coordinates of the system (i.e., the nodal positions of the finite element mesh) due to two reasons. First, constraints are nonlinear, and we locally linearize them in each simulation step. Second, we enforce constraints using the method of Lagrange multipliers, which applies forces in the direction normal to the constraints.

Taking the derivatives of Eqs. (11)-(12) w.r.t. a node $\mathbf{x}_n$ requires computing the derivatives of s_i and $\mathbf{V}^T$ w.r.t. $\mathbf{x}_n$. For the differentiation of s_i, we show in [PCH*13] that:

$$\frac{\partial s_i}{\partial \mathbf{x}_n} = \mathbf{r}_n \mathbf{v}_i \mathbf{u}_i^T. \qquad (13)$$

Papadopoulo and Lourakis [PL00] define the derivative of $\mathbf{V}$ w.r.t. each component g_{kl} of the deformation gradient $\mathbf{G}$ as:

$$\frac{\partial \mathbf{V}}{\partial g_{kl}} = -\mathbf{V}\Omega_v^{k,l}, \qquad (14)$$

where $\Omega_v^{k,l}$ is found by solving a 2×2 linear system for each g_{kl}. Since we need the derivative of the transpose of $\mathbf{V}$, and knowing that $\Omega_v^{k,l}$ is antisymmetric, we have:

$$\frac{\partial \mathbf{V}^T}{\partial g_{kl}} = \Omega_v^{k,l} \mathbf{V}^T. \qquad (15)$$

We can now use the chain rule to get the derivatives w.r.t. tetrahedral nodes $\mathbf{x}_n$. To avoid dealing with rank-3 tensors, we directly formulate the derivatives of $\mathbf{V}^T \mathbf{e}_j$ instead:

$$\frac{\partial \mathbf{V}^T \mathbf{e}_j}{\partial \mathbf{x}_n} = \sum_l \left(\Omega_v^{1,l} \mathbf{V}^T \mathbf{e}_j \quad \Omega_v^{2,l} \mathbf{V}^T \mathbf{e}_j \quad \Omega_v^{3,l} \mathbf{V}^T \mathbf{e}_j \right) \cdot \mathbf{r}_{n,l}. \qquad (16)$$

Using Eq. (13) and Eq. (16), we can compute the derivatives of the constraints in Eqs. (11)-(12) w.r.t. the nodal positions

of the mesh:

$$\frac{\partial C_{\min}^{i,j}}{\partial \mathbf{x}_n} = (s_i - 1)sign(\mathbf{e}_i^T \mathbf{V}^T \mathbf{e}_j)\mathbf{e}_i^T \frac{\partial \mathbf{V}^T \mathbf{e}_j}{\partial \mathbf{x}_n} + |\mathbf{e}_i^T \mathbf{V}^T \mathbf{e}_j| \frac{\partial s_i}{\partial \mathbf{x}_n}, \qquad (17)$$

$$\frac{\partial C_{\max}^{i,j}}{\partial \mathbf{x}_n} = (1 - s_i)sign(\mathbf{e}_i^T \mathbf{V}^T \mathbf{e}_j)\mathbf{e}_i^T \frac{\partial \mathbf{V}^T \mathbf{e}_j}{\partial \mathbf{x}_n} - |\mathbf{e}_i^T \mathbf{V}^T \mathbf{e}_j| \frac{\partial s_i}{\partial \mathbf{x}_n}. \qquad (18)$$

4. Simulation Algorithm

In Perez et al. [PCH*13], we describe our algorithm for simulating deformation dynamics with strain limiting. We formulate the simulation as a constrained optimization problem, namely a linear complementarity problem, and we apply standard solvers.

Given the nodal positions and velocities at the beginning of a simulation step, we perform an unconstrained dynamics step by integrating the unconstrained dynamics equations with backward Euler implicit integration and linearized forces. We then check whether strain-limiting constraints are violated. We formulate the constraints using Eqs. (11)-(12), and linearize them at the beginning of the simulation step using the constrain jacobians in Eqs. (17)-(18).

The resulting linear complementarity problem (LCP) is solved using projected Gauss-Seidel (PGS) relaxation [CPS92]. Frictional contact is incorporated by computing non-penetration constraints with contact friction using Coulomb's model. Contact constraints are linearized and seamlessly combined with strain-limiting constraints, and the entire constraint set is solved simultaneously.

5. Results and Discussion

In this section, we present a set of simulation scenarios to illustrate and qualitatively assess our anisotropic strain-limiting approach. We also compare our work with simple but naïve ways of addressing anisotropic strain limiting, such as orthogonal projection and linear interpolation of limits.

Simulations were run on a 3.4 GHz Quad-core Intel Core i7-3770 CPU with 32GB of memory.

5.1. Animation Tests

In order to qualitatively test the effect of anisotropic strain limiting, we ran different simulations with a $1\text{m} \times 0.2\text{m} \times 0.2\text{m}$ beam, fixed at one of its ends, with 200 tetrahedra, and a mass density of 1,000 Kg/m^3. Fig. 2 (middle) shows the results for a highly compliant beam (Young modulus of $E = 5\text{kPa}$) with anisotropic strain limiting (unrestricted deformation in the horizontal axis and restricted to 4% stretch and compress in the other two axes). For comparison, on the right we show the same beam with isotropic 4% strain
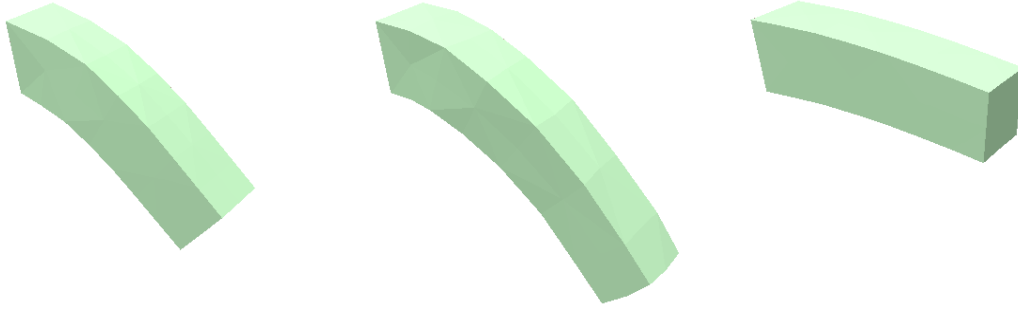
Figure 2: *A deformed beam with three different materials. From left to right: stiff without restrictions (E = 200kPa), compliant anisotropic (E = 5kPa, without restriction in the horizontal axis and 0.96 < s_i < 1.04 in the other two), and compliant isotropic (E = 5kPa, 0.96 < s_i < 1.04 in all axes).*

limiting, and on the left a stiffer unrestricted beam (E = 200kPa) with similar vertical deformation. Besides being significantly more stretched than the others, the anisotropic beam manages to preserve its wobbly elastic behavior along its main axis due to its very low stiffness and its lack of restriction, as observed in the video accompanying this paper.

A real-world finger is a clear example of anisotropic nonlinear elastic behavior, particularly under compression. Due to the presence of skin, flesh and bones, it is very compliant under light loading, but soon becomes almost rigid. This is true when the fingertip is pressed flat against a surface. When pressed on the side, there is hardly any deformation, showing a high anisotropy.

We simulate these highly nonlinear, highly anisotropic conditions using a finger model of approximately 7cm with 347 tetrahedra, simulated with a mass density of 1,000 Kg/m³ (roughly the average mass density of human flesh), and a Young modulus of E = 2MPa. The finger model is initialized with its longitudinal direction aligned with the horizontal axis ($\mathbf{e}_1$), and the nail facing up along the vertical axis ($\mathbf{e}_2$). Limits are defined as 0.95 < s_1 < 1.05 (stiff along $\mathbf{e}_1$), 0.75 < s_2 < 1.25 (compliant along $\mathbf{e}_2$) and 0.98 < s_3 < 1.02 (almost incompressible along $\mathbf{e}_3$). The aforementioned simulation parameters were selected by trial and error to approximately match the behavior of a real finger. Fig. 3 shows some results of the deformations when the finger is pressed against a table along each axis. We compared our model with an isotropic model using 0.75 < s_1 < 1.25. As expected, for the same motions we obtained similar results along ($\mathbf{e}_2$), and overly compliant behavior along the other axes. The differences across the models are clearly visible in the accompanying video.

Regarding performance, our approach is currently quite expensive. However, we have not tried to optimize the convergence of the solver. In the scenarios presented above, the simulation runs in real-time for a low number of constraints

($\sim$< 5) and drops below interactive rates for highly constrained configurations. In the finger scenarios, the framerate dropped below 1Hz during highly constrained motions (more than 40 tetrahedra with constraints).

5.2. Comparison with Other Approaches

In order to justify the use of our hyperbolic projection function for the computation of limits along an arbitraty direction, in this section we show that straightforward approaches do not yield correct results. We compare our hyperbolic projection method with the two simple but naïve approaches among the projection and the interpolation categories: orthogonal projection and linear interpolation.

Orthogonal projection works by simply rotating the limits defined in the global frame to frame F_d, and then projecting these limits onto the axes of F_d, where the deformation values are defined. Therefore, there is a total of 18 limits and constraints, as in our approach, with three stretch limits $s\_orthoproj_{max}^{j,i}$ and three compress limit $s\_orthoproj_{min}^{j,i}$ per principal axis of deformation:

$$s\_orthoproj_{\min}^{j,i} = 1 + (s_{\min}^j - 1)\,|\mathbf{e}_i^T \mathbf{V}^T \mathbf{e}_j|, \qquad (19)$$

$$s\_orthoproj_{\max}^{j,i} = 1 + (s_{\max}^j - 1)\,|\mathbf{e}_i^T \mathbf{V}^T \mathbf{e}_j|. \qquad (20)$$

Linear interpolation, on the other hand, interpolates the values defined in the global frame to find the limits along an arbitrary direction. Instead of rotating the global frame to F_d, we proceed the other way around: we apply the inverse rotation to F_d to get the principal axes of deformation in the global frame. This allows us to easily compute the interpolations by simply computing the intersection of the line defined by each principal axis of deformation with the ellipsoid defined by the global frame and its limits. Therefore, there is a total of 6 limits and constraints, as in the isotropic

Figure 3: *A finger is pressed against a table in three different configurations. Top: the finger has anisotropic limits simulating the behavior of a real finger (compliant when pressed flat, stiff otherwise). Bottom: the finger with isotropic compliant limits.*

case, with a stretch limit $s\_linearint^i_{max}$ and a compress limit $s\_linearint^i_{min}$ per principal axis of deformation:

$$s\_linearint^i_{min} = \left\| \begin{pmatrix} s^1_{min} & 0 & 0 \\ 0 & s^2_{min} & 0 \\ 0 & 0 & s^3_{min} \end{pmatrix} \mathbf{V}\,\mathbf{e}_i \right\|, \quad (21)$$

$$s\_linearint^i_{max} = \left\| \begin{pmatrix} s^1_{max} & 0 & 0 \\ 0 & s^2_{max} & 0 \\ 0 & 0 & s^3_{max} \end{pmatrix} \mathbf{V}\,\mathbf{e}_i \right\|. \quad (22)$$

We highlight the limitations of both aforementioned approaches in the simple scenario of a compliant vertical beam ($E = 10$kPa), fixed at its bottom, and compressing due to gravity, shown in Fig. 4. Poisson's ratio is set to $\nu = 0.3$. The vertical axis and one of the transverse axes are unrestricted. The remaining transverse axis can only deform up to 5% (i.e., $0.95 < s_i < 1.05$). Fig. 4 shows the state of the beam when a constraint is violated for the first time for orthogonal projection (left), our approach (middle), and linear interpolation (right).

In the case of orthogonal projection, constraints are already violated during the first frame of simulation, thus clearly yielding an overly stiff material. The reason behind this erroneous behavior is the absence of weights to reduce the influence of the limits defined on axes that are far from the principal axes of deformation. In our scenario, the SVD decomposition computed a vertical principal axis of deformation matching the global vertical axis. Therefore, the other two global axes, where stretch and compress limits are defined, are orthogonal to the vertical principal axis of deformation. Since the orthogonal projection between orthogonal axes is zero, according to Eqs. (19)-(20) there are two stretch

and two compress limits on the vertical principal axis of deformation that are equal to 1, meaning that no deformation is allowed along that axis. The beam is therefore frozen in its initial configuration.

In the case of linear interpolation, constraints are violated very late, when the beam has almost completely collapsed on itself and artifacts start to appear, clearly beyond the expected 5% maximal transversal deformation. This is due to the weighted combination of unrestrictive limits and very restrictive ones. Since values are interpolated, the very restrictive limit (in this case, the 5% limit) is progressively relaxed to the unrestritive limit as the principal axis of deformation moves from the restricted to the unrestricted axis. Since in this vertical beam scenario the rotation $\mathbf{V}$ resulted in a 180-degree rotation around the vertical axis, the transversal unrestrictive limit overly relaxed the transversal restrictive limit, thus resulting in an overly compliant material.

When using our approach, the state of the beam is coherent with the 5% transversal deformation limit.

6. Conclusion

In this paper, we have presented a model for simulating anisotropic behaviors in highly nonlinear elastic materials using strain-limiting constraints. The core novelty of our approach is the use of a hyperbolic projection method to compute limits along any deformation direction given a set of limits defined in the global axes. Using our model, we are able to simulate the highly anisotropic and non-linear elastic behavior of a finger, which is initially compliant when pressed flat against a surface but extremely stiff when pressed on the side. We compared our projection method with simple solutions such as orthogonal projection or linear
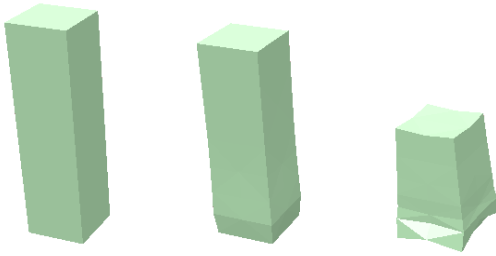
Figure 4: *State of a deforming beam when the first constraint violation is detected, for different ways of computing the limits. The beam ($E = 10kPa$, $\nu = 0.3$) is resting on the floor and is compressing under gravity. The vertical axis and one of the transverse axes are unrestricted. The remaining transverse axis can deform up to 5% ($0.95 < s_i < 1.05$). From left to right: orthogonal projection, hyperbolic projection (our approach), and linear interpolation.*

interpolation, and showed that our approach produces predictable and more realistic results.

Nevertheless, our hyperbolic projection approach exhibits some limitations, since it does not exactly preserve the limits in the case of isotropic behavior. If the principal deformation axes do not match the global axes, limits are scaled as expected according to the angle between the axes. In an isotropic scenario, however, limits should not be scaled since they are the same for every direction. In the worst case scenario (half-way between axes, i.e., an angle of 45 degrees), the compress limit, for instance, is equal to $1 + (s_{min} - 1)\sqrt{2}$ instead of simply s_{min}.

In addition, we observed some cases of locking when the limits were too restrictive, resulting in an overconstrained system. Future work will address these locking issues, as well as investigate ways of limiting other deformation modes such as shear. In addition, we would like to automatically estimate and place anisotropic limits in a given model using real-world measurements [BBO*09], thus avoiding ad-hoc tuning and improving the quality of the deformations. Finally, we would like to explore the use of more efficient solvers, ideally reaching interactive rates for high-resolution models.

Acknowledgements

References

[AMC09] ALLARD J., MARCHAL M., COTIN S.: Fiber-based fracture model for simulating soft tissue tearing. In *Proc. of Medicine Meets Virtual Reality (MMVR)* (2009). 2

[BBO*09] BICKEL B., BÄCHER M., OTADUY M. A., MATUSIK W., PFISTER H., GROSS M.: Capture and modeling of non-linear heterogeneous soft tissue. *ACM Trans. Graph. 28*, 3 (July 2009), 89:1–89:9. 7

[BMF03] BRIDSON R., MARINO S., FEDKIW R.: Simulation of clothing with folds and wrinkles. *Proc. of ACM SIGGRAPH / Eurographics Symposium on Computer Animation* (2003). 1, 2

[CPS92] COTTLE R., PANG J., STONE R.: *The Linear Complementarity Problem*. Academic Press, 1992. 4

[ITF04] IRVING G., TERAN J., FEDKIW R.: Invertible finite elements for robust simulation of large deformation. *Proc. of ACM SIGGRAPH/Eurographics Symposium on Computer Animation* (2004), 131–140. 2

[MG04] MÜLLER M., GROSS M.: Interactive virtual materials. *Proc. of Graphics Interface* (2004). 2

[PCH*13] PEREZ A. G., CIRIO G., HERNANDEZ F., GARRE C., OTADUY M. A.: Strain limiting for soft finger contact simulation. In *Proc. of IEEE World Haptics Conference* (2013). 2, 3, 4

[PDA03] PICINBONO G., DELINGETTE H., AYACHE N.: Non-linear anisotropic elasticity for real-time surgery simulation. *Graph. Models 65*, 5 (2003), 305–321. 2

[PL00] PAPADOPOULO T., LOURAKIS M. I. A.: Estimating the jacobian of the singular value decomposition: Theory and applications. In *European Conference on Computer Vision* (2000). 4

[Pro95] PROVOT X.: Deformation constraints in a mass-spring model to describe rigid cloth behavior. *Proc. of Graphics Interface* (1995). 1, 2

[SZL*11] SIN F., ZHU Y., LI Y., SCHROEDER D., BARBIČ J.: Invertible isotropic hyperelasticity using SVD gradients. In *ACM SIGGRAPH / Eurographics Symposium on Computer Animation (Posters)* (2011). 2

[TPS09] THOMASZEWSKI B., PABST S., STRASSER W.: Continuum-based strain limiting. *Computer Graphics Forum 28*, 2 (2009), 569–576. 1, 2

[WOR10] WANG H., O'BRIEN J., RAMAMOORTHI R.: Multi-resolution isotropic strain limiting. *Proc. of ACM SIGGRAPH Asia* (2010). 2